



## 2 Effects of pore collapse and grain crushing on 3 ultrasonic velocities and $V_p/V_s$

4 Jérôme Fortin,<sup>1</sup> Yves Guéguen,<sup>1</sup> and Alexandre Schubnel<sup>2</sup>

5 Received 20 August 2005; revised 13 February 2007; accepted 6 June 2007; published XX Month 2007.

6 [1] Compressional, shear wave velocities and their ratio,  $V_p/V_s$ , were measured along with  
7 porosity variations during wet and dry hydrostatic compaction of Bleurswiller sandstone, a  
8 25% porosity Vosgian sandstone. At first, increase in hydrostatic pressure was  
9 accompanied by a simultaneous increase of both  $V_p$  and  $V_s$  as expected. At a critical  
10 effective confining pressure  $P^*$ , a large mechanical decrease of porosity was observed that  
11 was due to pore collapse and grain crushing. Theoretically, two different processes are  
12 affecting the elastic wave velocities in counteracting ways during cataclastic compaction:  
13 cracking and porosity decrease. Our experimental results show that cracking is the  
14 dominant effect, so that grain crushing and porosity reduction were accompanied by a  
15 large decrease in velocities. The ratio  $V_p/V_s$  was also observed to change during our  
16 experiments: In the wet specimen,  $V_p/V_s$  value increased from 1.72 to 1.84, while in the  
17 dry specimen, it increased from 1.59 below  $P^*$  to 1.67 beyond  $P^*$ , respectively. To  
18 quantitatively interpret these results, an isotropic effective medium model (EM) was used  
19 that considered the sandstone as a mixture of spheroidal pores and penny-shaped cracks.  
20 In particular, the increase in  $V_p/V_s$ , in the wet case, is well reproduced and shows the  
21 important role played by the mechanical coupling of fluid with low aspect ratio cracks  
22 ( $<10^{-2}$ ). In the dry case, however, our experimental results highlight an increase of  $V_p/V_s$   
23 ratio during cataclastic compaction, in apparent contradiction with the predictions of  
24 the EM model. Indeed, increases in  $V_p/V_s$  ratio, and hence in Poisson's ratio, are, in  
25 general, attributed to fluid saturation. A closer look to the microstructure may provide a  
26 possible interpretation: Beyond  $P^*$ , grains are no longer cemented. Using Digby's granular  
27 model as an alternative model, we were able to reach a quantitative agreement with  
28 the experimental results. The possible implication is that in both dry and wet conditions,  
29 cataclastic compaction due to grain crushing induces an increase in  $V_p/V_s$  ratio.

30 **Citation:** Fortin, J., Y. Guéguen, and A. Schubnel (2007), Effects of pore collapse and grain crushing on ultrasonic velocities and  
31  $V_p/V_s$ , *J. Geophys. Res.*, 112, XXXXXX, doi:10.1029/2005JB004005.

### 33 1. Introduction

34 [2] Compaction can occur as a result of mechanical and  
35 chemical processes [Wong *et al.*, 2004; Lehner and Leroy,  
36 2004]. While chemical compaction usually becomes the  
37 dominant process at depths greater than 4.5 km [Giles,  
38 1997; Ramm, 1992], mechanical compaction involves the  
39 rearrangement of grains at lower depths. Mechanical com-  
40 paction and associated porosity reduction play an important  
41 role in the diagenesis of sandstones and they may also affect  
42 sandstone reservoirs during hydrocarbon production [Smits  
43 *et al.*, 1988; Fredrich *et al.*, 1998]. In such cases, mecha-  
44 nical compaction may occur because production decreases  
45 the pore pressure and hence increases the effective stress on  
46 the sandstone solid matrix. Results from hydrostatic com-  
47 paction experiments on a wide range of sands and sand-

stones are generally interpreted in terms of a critical 48  
pressure  $P^*$ , which characterizes the onset of homogeneous 49  
pore collapse and grain crushing (nonlocalized cataclastic 50  
flow) [Zhang *et al.*, 1990; Wong *et al.*, 1997]. 51

[3] Recent field [Mollema and Antonellini, 1996], and 52  
laboratory [Olsson, 1999; Klein *et al.*, 2001; Baud *et al.*, 53  
2004; Fortin *et al.*, 2005, 2006] observations have focused 54  
attention on the formation of localized compaction bands in 55  
porous sandstones. Laboratory experiments have shown that 56  
compaction bands occurred in sandstones with porosities 57  
ranging from 20 to 28%, deformed at room temperature, 58  
under a triaxial loading. The present investigation is res- 59  
tricted to conditions of zero deviatoric stress (purely hydro- 60  
static compaction) as the case of nonzero deviatoric stress in 61  
Bleurswiller sandstone has been previously reported by 62  
Fortin *et al.* [2005, 2006]. In such experimental conditions, 63  
compaction bands can theoretically not occur [Rudnicki, 64  
2004], and the deformation is assumed to be homogeneous 65  
(principle of symmetry). 66

[4] The measurement of elastic wave velocities has often 67  
been used to provide some information about the rock 68

<sup>1</sup>Laboratoire de Géologie, Ecole Normale Supérieure, Paris, France.

<sup>2</sup>Lassonde Institute, University of Toronto, Toronto, Ontario, Canada.

69 microstructure [e.g., *Nur and Wang*, 1989]. Being by nature  
 70 small mechanical perturbations, elastic waves are strongly  
 71 affected by the rock deformation processes. In consequence,  
 72 the behavior of the elastic wave velocities ( $V_p$  and  $V_s$ , and  
 73 their ratio  $V_p/V_s$ ) during pore collapse and grain crushing  
 74 is not straightforward. Indeed, elastic wave velocities can  
 75 be affected by two distinct and competitive mechanisms:  
 76 (1) cracking and (2) porosity reduction. In the first case, it is  
 77 well known that elastic wave velocities may be reduced  
 78 substantially during triaxial compression experiments in the  
 79 presence of cracks. This is observed in crystalline rocks  
 80 [e.g., *Hadley*, 1976], and also in porous rocks [e.g., *Scott*  
 81 *et al.*, 1993]. Under hydrostatic tests, *Zhang et al.* [1990]  
 82 and *Wong et al.* [1997] demonstrate from postmortem  
 83 microstructural observations that grain crushing in sand-  
 84 stone is generally characterized by extensive microcracking  
 85 as cracks nucleate and propagate when pressure reaches the  
 86 critical pressure  $P^*$ . Therefore these newly formed cracks  
 87 may induce a decrease in elastic wave velocities. Second,  
 88 *Zhang et al.* [1990], *Wong et al.* [1997], and *Karner et al.*  
 89 [2003] report for hydrostatic tests on porous sandstones,  
 90 that pore collapse can induce a porosity reduction higher  
 91 than 10%. Therefore porosity reduction may result in an  
 92 increase of the elastic wave velocities [*Dvorkin and Nur*,  
 93 1996; *Avseth et al.*, 1998].

94 [5] Understanding the stress dependencies of seismic  
 95 velocities is important for interpreting a variety of seismic  
 96 data. The velocity dependence on confining pressure can  
 97 be phenomenologically described [*Zimmerman et al.*,  
 98 1986; *Shapiro*, 2003] without specifying any microme-  
 99 chanical model. However, effective medium theories (EMT)  
 100 connect the effective elastic properties of a rock to that of the  
 101 solid matrix (pore- and crack-free), the fluid properties, and  
 102 parameters related to pores and cracks such as the crack  
 103 density  $\rho$  and the porosity  $p$ . Using EMT makes it possible to  
 104 specify a macroscopic behavior relying on a microscopic  
 105 mechanism. Two different approaches are frequently used in  
 106 EMT calculations: (1) one is the approximation of an effec-  
 107 tive matrix and (2) the other is the approximation of an  
 108 effective field. In the first case, each crack or pore is assumed  
 109 to be isolated in a medium that is the effective matrix  
 110 [*O'Connell and Budiansky*, 1974, 1977; *Salganik*, 1973;  
 111 *Hashin*, 1988]. For example, using a differential self-consis-  
 112 tent method, *Le Ravalec and Guéguen* [1996] calculated the  
 113 effective elastic moduli of a two-phase material: an isotropic  
 114 solid matrix containing an isotropic distribution of round  
 115 pores or oblate spheroidal cracks. In the second case, crack  
 116 interactions are accounted for through an effective stress. Of  
 117 special interest is the model of noninteraction approximation.  
 118 Indeed, using this assumption, the effective elastic properties  
 119 of a material containing fluid-filled pores of various shapes  
 120 can be calculated rigorously and exactly in a manner that  
 121 depends on the crack and pore distributions solely [*Bristow*,  
 122 1960; *Walsh* 1965; *Kachanov*, 1980; *Sayers and Kachanov*,  
 123 1995]. The noninteraction assumption, often wrongly con-  
 124 fused with the low crack density one, remains accurate at high  
 125 crack densities, provided the locations of crack centers are  
 126 random. Indeed, at a microscopic level, crack interactions  
 127 exist but are approximately compensated. *Sayers and Kacha-*  
 128 *nov* [1995] and *Schubnel and Guéguen* [2003] proved that  
 129 this assumption is the best one for certain distributions such  
 130 as random (isotropic) or aligned crack distributions. In such a

way, the effective elastic moduli of a material containing a  
 mixture of saturated pores and ellipsoidal cracks were given  
 recently by *Shafiro and Kachanov*, [1997]. In this model, the  
 effective stress is estimated using the scheme of Mori-Tanaka  
 (let us point out that if the material contains only cracks, the  
 Mori-Tanaka scheme corresponds exactly to the noninterac-  
 tion assumption).

[6] In this paper, we report experimental results obtained  
 during the hydrostatic compaction of dry and saturated  
 specimens of Bleurswiller sandstone (a Vosgian sandstone  
 with an initial porosity  $p = 25\%$ ). Elastic wave velocities ( $V_p$   
 and  $V_s$ , and their ratio  $V_p/V_s$ ) were measured during these  
 experiments: In the first parts of the loading, the application  
 of the hydrostatic pressure closes the preexisting cracks and  
 pores with large aspect ratios and raises the velocities.  
 However, our data show that during pore collapse and grain  
 crushing, elastic wave velocities decrease, which implies  
 that they are more affected by cracks than by porosity  
 reduction. To interpret theoretically and quantitatively these  
 results, we consider a porous rock as made of a mixture of  
 solid grains, spherical pores, and penny-shaped cracks. The  
 effective medium model “pores and cracks” that we used  
 here both in dry and fluid-saturated conditions, is based on  
 the works of *Kachanov* [1993], *Kachanov et al.* [1994], and  
*Shafiro and Kachanov* [1997].

## 2. Experimental Methods

### 2.1. Sample

[7] Cylindrical specimens of 80 mm in length and  
 40 mm in diameter were prepared from Bleurswiller  
 sandstone. This sandstone was collected from the quarry  
 of Frain (Vosges, eastern France) and is identical to the  
 one previously studied by *Fortin et al.* [2005, 2006].  
 Figure 1a gives a picture of an intact specimen. The  
 physical properties are detailed in Table 1. Porosity is  
 about 25%. *Fortin et al.* [2006] have investigated micro-  
 structure using optical microscopy: This gray sandstone  
 contains  $\sim 50\%$  quartz,  $\sim 30\%$  feldspars, and  $\sim 20\%$   
 oxides-micas and grain sizes range from 80  $\mu\text{m}$  to  
 150  $\mu\text{m}$  with a mean value of 110  $\mu\text{m}$ . Figure 1b show  
 a scanning electron microscopy (SEM) of an intact speci-  
 men, for comparison: Porosity appears in black, and quartz  
 grains appear darker than the feldspar grains. Grains are  
 mostly subangular to subrounded. Clay is often located  
 within the pores, or between two grains. The microstruc-  
 ture analysis does not reveal any layering. Moreover, the  
 undeformed sample has an initial  $P$  wave velocity aniso-  
 tropy lower than 1.5%. We assume in the following that  
 Bleurswiller sandstone is isotropic.

### 2.2. Laboratory Equipment

[8] The triaxial cell installed at the Laboratoire de Géolo-  
 gie of Ecole Normale Supérieure (Paris, France) was used  
 to investigate the evolution of the elastic wave velocities in  
 Bleurswiller sandstone deformed under hydrostatic loading.  
 A schematic diagram of the apparatus is shown in Figure 2.  
 The confining pressure is servo-controlled with an accuracy  
 of 0.1 MPa and can reach 300 MPa. The confining medium  
 is oil. The axial load can be achieved through an autocom-  
 pensated hydraulic piston, but it was not used in the  
 experiments presented in this study since we focus here



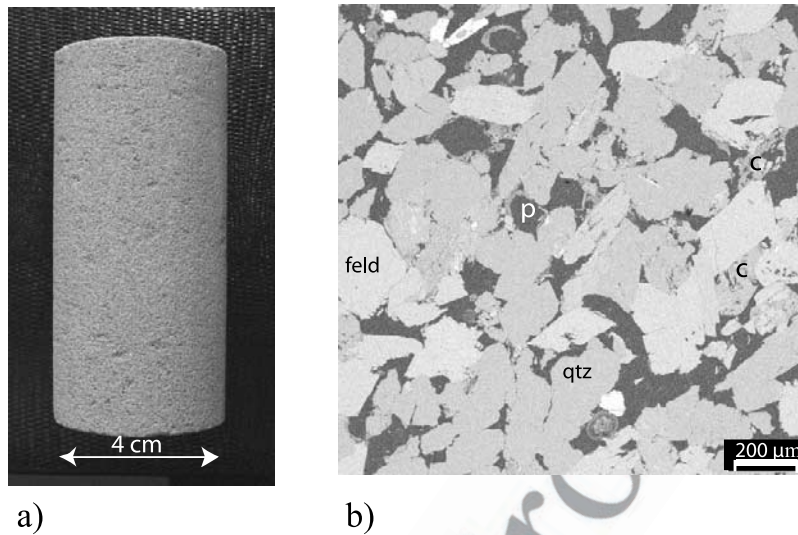


**Figure 1.** (a) Picture of a nondeformed sample of Bleurswiller sandstone. (b) SEM micrograph (backscattered) of an intact sandstone. Epoxy-filled pores appear in black; porosity is about 25%. SEM micrograph (backscattered) of an intact sandstone. Epoxy-filled pores (p) appear in black, porosity is about 25%. Quartz, feldspar, and clay are denoted by qtz, feld, and c, respectively.

190 on hydrostatic compaction with zero deviatoric stress. Pore  
 191 pressure can be driven by two precision volumetric pumps.  
 192 Pore fluid is introduced into the sample through hardened  
 193 steel end pieces placed on the top and bottom of the rock  
 194 sample. Maximum pore pressure in the system is 100 MPa.  
 195 Both pumps can be controlled either in pressure (0.01 MPa  
 196 precision), in flow (minimum flow is  $0.1 \text{ cm}^3 \text{ h}^{-1}$ ) or in  
 197 volume (precision approximately  $0.005 \text{ cm}^3$ ). The main  
 198 advantage of the triaxial apparatus is its 34 electric feed-  
 199 throughs that can allow simultaneously measurements  
 200 of ultrasonic  $P$  and  $S$  velocities, as well as local strains  
 201 (strain gauges).

### 202 2.3. Strain Measurements

203 [9] The results of dry and wet experiments are presented  
 204 in this study. In the dry experiment, volumetric strain  $\varepsilon_v$   
 205 was calculated from axial strain  $\varepsilon_z$  and radial strain  $\varepsilon_r$  using  $\varepsilon_v =$   
 206  $2\varepsilon_r + \varepsilon_z$ . Measurements were acquired using strain gauges  
 207 (TML FLA-20, Tokyosokki) directly glued to sample's  
 208 surface (Figure 3a). Each of strain gauge was mounted in  
 209 a 1/4 Wheatstone bridge. Uncertainty in strain measurement  
 210 was approximately  $10^{-5}$ . Given that pores are much more  
 211 compliant than solid grains, we assume that volumetric  
 212 strain was equal to change in porosity.

213 [10] In the wet experiment, the sample was deformed  
 214 under drained conditions at a constant pore pressure of  
 215 10 MPa. Pore pressure was maintained constant, and pore  
 216 volume variation throughout the experiment was recorded  
 217 using a volumeter, allowing a monitoring of the evolu-  
 218 tion of sample connected porosity. In this case, radial strain  
 219  $\varepsilon_r$  was determined using  $\varepsilon_r = \varepsilon_v/3$ .

### 220 2.4. Velocity Measurements

221 [11] Velocities are obtained using a pulse transmission  
 222 method in which measured traveltimes of elastic wave  
 223 through the rock and sample length, corrected from radial  
 224 deformation, are used to calculate the velocities.  $P$  and  $S$   
 225 elastic wave velocities were measured perpendicular to

axis-symmetric axis, along diameter of the sample 226  
 (Figure 3a). To record  $P$  wave velocities we used source- 227  
 receiver lead-zirconate piezoceramic discs (PZT) 10 mm in 228  
 diameter and 1 mm in thickness (PI255, PI ceramics, 229  
 resonant frequency of 1 MHz). Shear wave PZTs were plate 230  
 $10 \times 10 \times 1$  in dimension.  $P$  and  $S$  wave PZTs were glued 231  
 directly onto the sample surface and positioned with approx- 232  
 imately 0.5 mm accuracy, while the distance between 233  
 opposite (paired) PZTs from which the velocities were 234  
 calculated was measured within 0.01 mm. The sending 235  
 transducers are driven by a Dirac pulse, generated by a 236  
 Sofranel<sup>®</sup> generator (approximately 370 V at 1 MHz fre- 237  
 quency). The elastic wave produced by the first transducer 238  
 is transmitted through the sample and detected by the 239  
 second transducer. The resulting signals were recorded on 240  
 an oscilloscope (Tektronix TDS-460A) and averaged over 241  
 50 waveforms. The oscilloscope digitized the averaged trace 242  
 with 2500 points at a time sweep of  $25 \mu\text{s}$ , thus allowing a 243  
 time resolution of 10 ns. Then, the averaged signal is 244  
 transferred to a laboratory computer for further processing. 245  
 An example of received  $S$  waveforms, at different confining 246  
 pressure is shown in Figure 3b. Traveltimes were deter- 247  
 mined using a double picking technique, i.e., the mean 248  
 between (1) the first arrival and (2) the first peak of the 249  
 signal, minus a quarter of period (Figure 3b). Traveltime 250  
 calibration was accomplished by using aluminium rods of 251  
 different lengths. In such conditions, the error in absolute 252

**Table 1.** Physical Properties of Bleurswiller Sandstone Used in t1.1  
 This Study

Property	Value	t1.2
Porosity	25%	t1.3
Grain size, $\mu\text{m}$	80–180	t1.4
Permeability, $\times 10^{-16} \text{ m}^2$	200	t1.5
Initial $P$ wave anisotropy, %	<1.5	t1.6

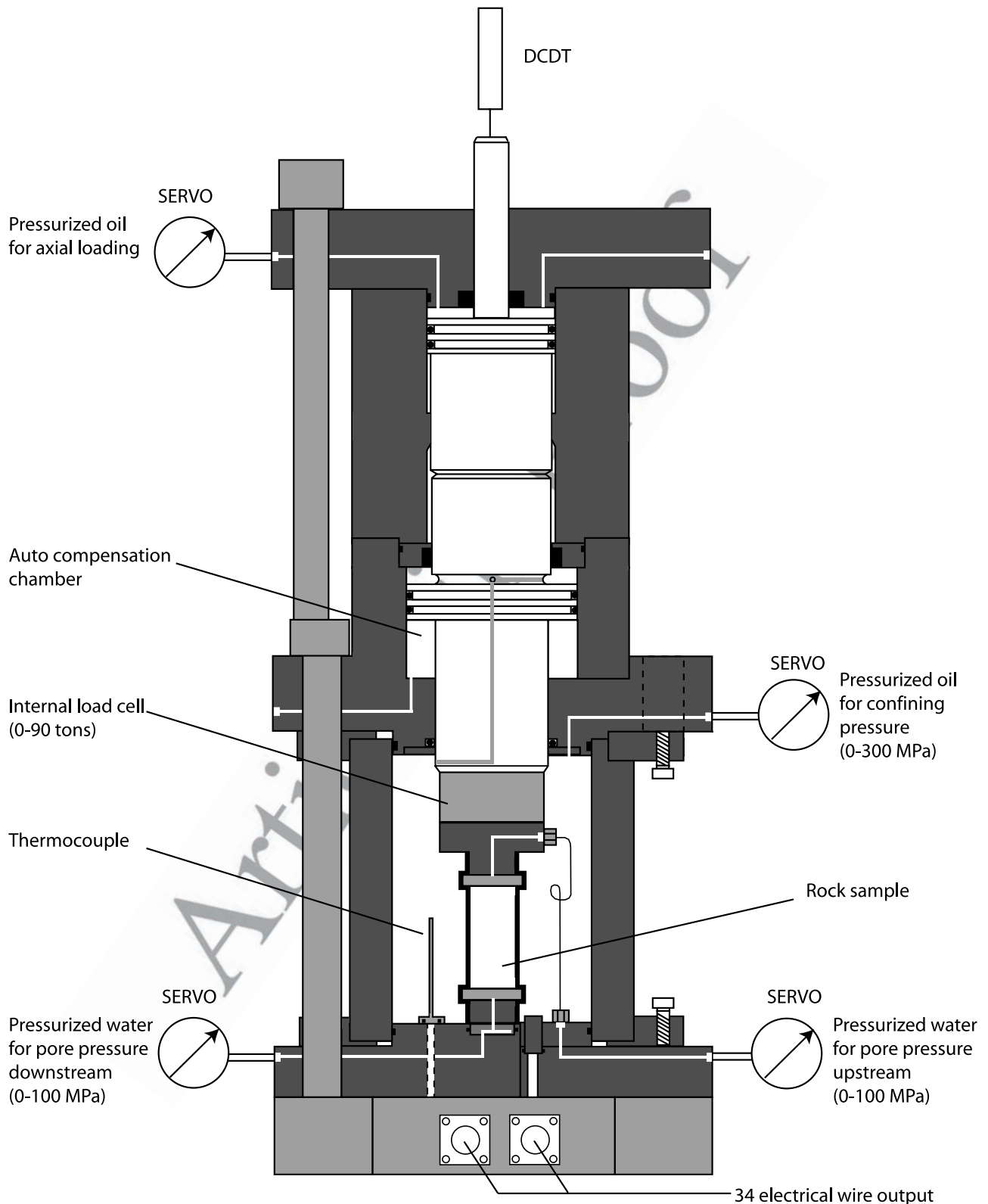


**Figure 2.** Schematic diagram of the triaxial high-pressure cell installed at the Laboratoire de Géologie of Ecole Normale Supérieure of Paris (France).

253 velocity is estimated to be less than 3%, but relative error  
 254 between two consecutive measurements was reduced to  
 255 0.5%. Finally,  $P$  wave velocities (and  $S$  wave velocities)  
 256 were determined using the average of values calculated

along the two perpendicular trajectories (Figure 3a). In the 257  
 same way, the ratio  $V_p/V_s$  was calculated as the average of 258  
 the two ratios  $t_s/t_p$  (traveltimes), measured along the two 259  
 perpendicular trajectories. 260

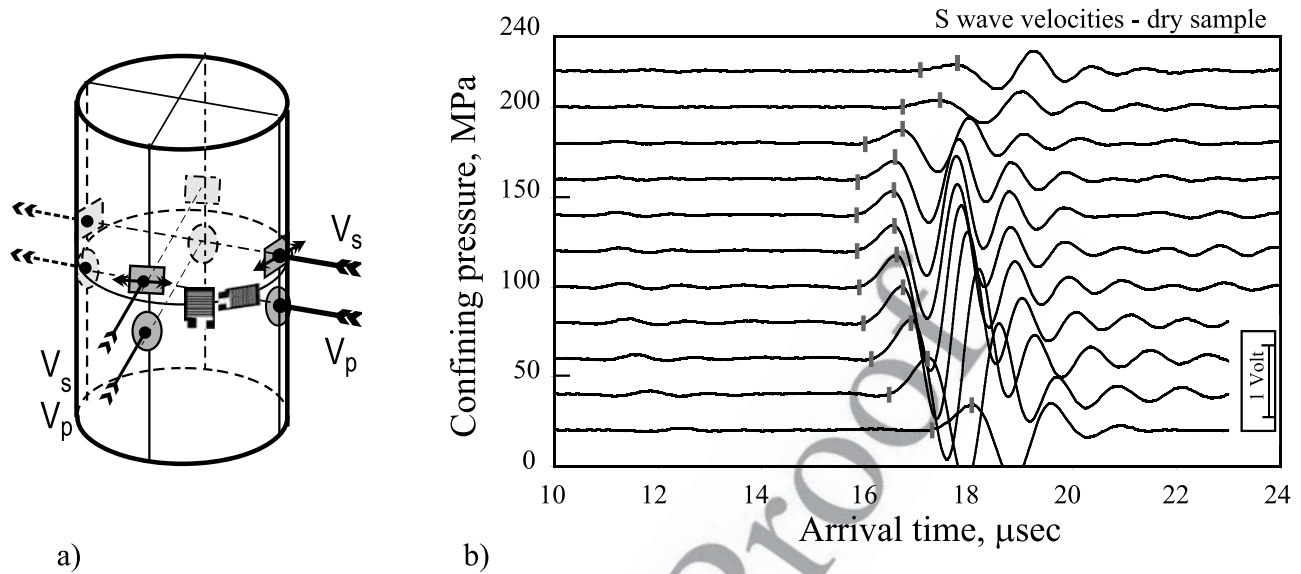


**Figure 3.** (a) Sample setup used in this study. The initial sample diameter and length were 40 mm and 80 mm, respectively. The velocities  $P$  and  $S$  were measured perpendicular to the main axis of the specimen. The PZT and strain gages were directly glued on the rock. (b) Example of received  $S$  waveforms at different confining pressures obtained in the dry experiment.

## 261 2.5. Experimental Procedure

262 [12] Two experiments, one in dry conditions, the other in  
 263 wet conditions, were carried out under hydrostatic loading  
 264 at a confining pressure up to 280 MPa. Inside the vessel, the  
 265 sample was covered with a Neoprene jacket that insulated it  
 266 from the confining oil.

267 [13] The dry sample was air dried at  $50^{\circ}\text{C}$  for 48 hours.  
 268 The wet sample was immersed in tap water for 48 hours to  
 269 ensure complete saturation before measurement. During the  
 270 wet experiment, confining pressure was first increased to  
 271 5 MPa. Pore pressure and confining pressure were then  
 272 raised up simultaneously to 1 and 6 MPa, respectively.  
 273 Pressure was held constant for at least 12 hours to obtain  
 274 full fluid saturation of the sample. At the beginning of the  
 275 wet experiment, pore pressure and confining pressure were  
 276 raised up to 10 and 20 MPa, respectively.

277 [14] During both experiments, confining pressure was  
 278 varied in step of 5 MPa and the pressurization ramp is  
 279  $\sim 0.05 \text{ MPa s}^{-1}$ . At the end of each step, confining  
 280 pressure was kept constant over a period of either 15 min  
 281 (“during elastic compaction”) or 60 minutes (“during  
 282 cataclastic compaction”). These delays are required for  
 283 two reasons: (1) they allow the changes in pore structure  
 284 to stabilize during cataclastic compaction [Zhang *et al.*,  
 285 1990], and (2) as noted by Gardner *et al.* [1965] and  
 286 Christensen and Wang [1985], there is a slow velocity  
 287 drift, as the time for velocity stabilization is linked to the  
 288 pore structure, the clay content, and the mineral contacts.  
 289 Two examples of the evolution of the  $P$  wave velocity  
 290 (wet experiment) versus time are given in Figure 4. In  
 291 Figure 4a, when effective pressure is increased from 25 to  
 292 30 MPa (dashed curve), the velocity increases drastically  
 293 by  $25 \text{ m s}^{-1}$  in 3 min and then increases slowly by less  
 294 than  $10 \text{ m s}^{-1}$  in 10 min. After 15 min, the velocity is not  
 295 totally stabilized, but its variations are small in comparison  
 296 with the amplitude of the error bar (0.5%, which corres-

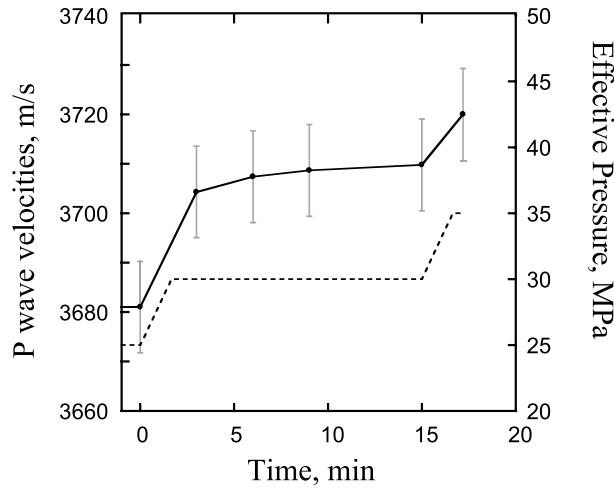
ponds to  $20 \text{ m s}^{-1}$ ). Figure 4b gives the evolution of the  
 297  $P$  wave velocities during the cataclastic compaction of  
 298 the sample: When effective pressure is increased from 135  
 299 to 140 MPa (dashed curve), the velocity decreases. After  
 300 50 min, the velocity is stabilized, which allowed us to  
 301 increase the effective pressure from 140 to 145 MPa after  
 302 a step duration of 60 min. 303

[15] At the end of each experiment, the sample was  
 304 carefully unloaded at decreasing confining pressure with  
 305 10 MPa decrements and recovered for microstructural  
 306 analysis. 307

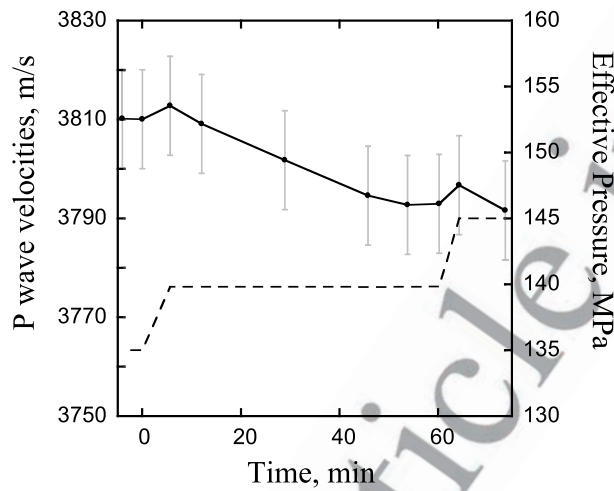
## 3. Theoretical Background 309

### 3.1. General Relations for Elastic Energy of Cracked and Porous Rock 310-311

[16] In porous rocks, changes in porosity alone are not  
 312 sufficient to account quantitatively for the evolution of  
 313 elastic properties. Because microcracks are very compliant,  
 314 they have a major effect on elastic properties although they  
 315 represent an extremely small amount of porosity, typically  
 316 less than 1%. In porous rocks microcracks may be thought  
 317 of as representatives of narrow gaps due to asperities in  
 318 grain-to-grain contacts. Our choice of approximations  
 319 (a model considering a mixture of spheroidal pores and  
 320 penny-shaped cracks) results from a compromise between  
 321 models simple enough to get closed forms for elastic  
 322 moduli, and yet sophisticated enough to capture the key  
 323 physical processes. Using Kachanov [1993] and Shafiro  
 324 and Kachanov [1997], the effective elastic properties may  
 325 be expressed in a unique manner as a function of the  
 326 overall porosity  $p$  and the crack density  $\rho$ . The crack  
 327 density is defined as  $\rho = 1/V \sum_{i=1}^N c_i^3$ , where  $c_i$  is the radius  
 328 of the  $i$ th crack and  $N$  is the total number of cracks  
 329 embedded in the representative elementary volume (REV)  
 330  $V$ . The elastic potential  $f(\sigma)$  for a given tensor stress state  
 331



a) Wet Sample (Time dependance of P-wave velocities during 'elastic compaction')



b) Wet Sample (Time dependance of P-wave velocities during 'cataclastic compaction')

**Figure 4.** Time dependence of  $P$  wave velocities. (a) Elastic compaction. When effective pressure is increased from 25 to 30 MPa (dashed curve), the velocity stabilized after 15 minutes. (b) Cataclastic compaction. When effective pressure is increased from 135 to 140 MPa (dashed curve), the velocity decreases; however, after 50 min, the velocity is stabilized, which allowed us to increase the effective pressure from 140 to 145 MPa after a step duration of 60 min.

332  $\sigma$  (from which the macroscopic volume-averaged strains  
333 are obtained as  $\varepsilon_{ij} = \partial f / \partial \sigma_{ij}$ ) may be written as a sum:

$$f = f_o + \Delta f, \quad (1)$$

335 where  $f_o = 1/2E_o[(1 + \nu_o)\text{tr}(\sigma \cdot \sigma) - \nu_o(\text{tr} \sigma)^2]$  is the  
336 potential of the bulk material ( $E_o\nu_o$  are its Young's modulus  
337 and Poisson's ratio;  $\text{tr}(\sigma \cdot \sigma) = \sigma_{ij}\sigma_{ji}$  and  $(\text{tr} \sigma)^2 = (\sigma_{kk})^2$ ),  
338 and  $\Delta f$  is the additional term due to pores and cracks. The

elastic potential  $\Delta f$  can be expressed as a sum [Kachanov, 339  
1993]: 340

$$\Delta f = \frac{1}{\Gamma} (\Delta f_{\text{nonint}}^{\text{pores}} + \Delta f_{\text{nonint}}^{\text{cracks}}). \quad (2)$$

The second term in the parentheses is the potential 342  
associated to noninteracting cracks. In the crack case, as 343  
discussed by Kachanov [1993], Sayers and Kachanov 344  
[1995], and Schubnel and Guéguen [2003], the noninterac- 345  
tion scheme is valid up to crack density of at least 0.5. The 346  
first term in the parentheses is the potential associated to 347  
noninteracting pores. The effect of stress interactions 348  
between pores is taken into account in the term  $\Gamma$ . In the 349  
dry case,  $\Gamma = 1 - p$  where  $p$  is the overall porosity [e.g., 350  
Kachanov, 1993]. This approach corresponds to Mori- 351  
Tanaka's model [Mori and Tanaka, 1973]. The interaction 352  
effect between cracks and pores is "asymmetric": cracks do 353  
no affect pores, whereas pores affect cracks. In the case 354  
where the rock is fluid saturated, the effect of stress 355  
interactions due to spheroidal pores can be neglected and 356  
 $\Gamma = 1$ . 357

[17] Kachanov [1993] gives the expression of the elastic 358  
potential associated with randomly oriented noninteracting 359  
cracks: 360

$$\Delta f_{\text{nonint}}^{\text{cracks}} = \rho \frac{h}{2E_o} \left\{ \text{tr}(\sigma \cdot \sigma) - \frac{1}{5} \left[ 1 - \left( 1 - \frac{\nu_o}{2} \right) \frac{\delta}{1 + \delta} \right] \right. \\ \left. \times \left( 2 \text{tr}(\sigma \cdot \sigma) + (\text{tr} \sigma)^2 \right) \right\}, \quad (3)$$

where  $h$  is a factor describing the penny-shaped geometry, 362

$$h = \frac{16(1 - \nu_o^2)}{9(1 - \nu_o/2)}. \quad (4)$$

Typically,  $h \simeq 2$ . The  $\delta$  characterizes the coupling between 364  
the solid stress and the fluid pressure, and thus determines 365  
the fluid impact on the effective crack compliance: 366

$$\delta = (1 - \nu_o/2) \frac{E_o \zeta}{K_f} h, \quad (5)$$

$\delta$  compares the fluid bulk modulus  $K_f$  to what is an apparent 367  
crack bulk modulus  $(1 - \nu_o/2)E_o\zeta h$ , where  $\zeta$  is the crack 368  
aspect ratio, which is the ratio between the aperture to the 370  
diameter. In the dry case  $\delta \rightarrow \infty$  [e.g., Kachanov, 1993; 371  
Schubnel and Guéguen, 2003]. 372

[18] An expression of the elastic potential associated to 373  
noninteracting spheroidal pores is proposed by [Shafiro and 374  
Kachanov, 1997] 375

$$\Delta f_{\text{nonint}}^{\text{pores}} = p \frac{3(1 - \nu_o)}{4E_o} \left\{ \frac{10(1 + \nu_o)}{7 - 5\nu_o} \text{tr}(\sigma \cdot \sigma) \right. \\ \left. - \left[ \frac{1 + 5\nu_o}{7 - 5\nu_o} + \frac{1}{3(1 + \delta_s)} \right] (\text{tr} \sigma)^2 \right\}, \quad (6)$$

where  $\delta_s$  incorporates the following physical parameters: the 376  
matrix stiffness, which is the stiffness of the solid portion, 378



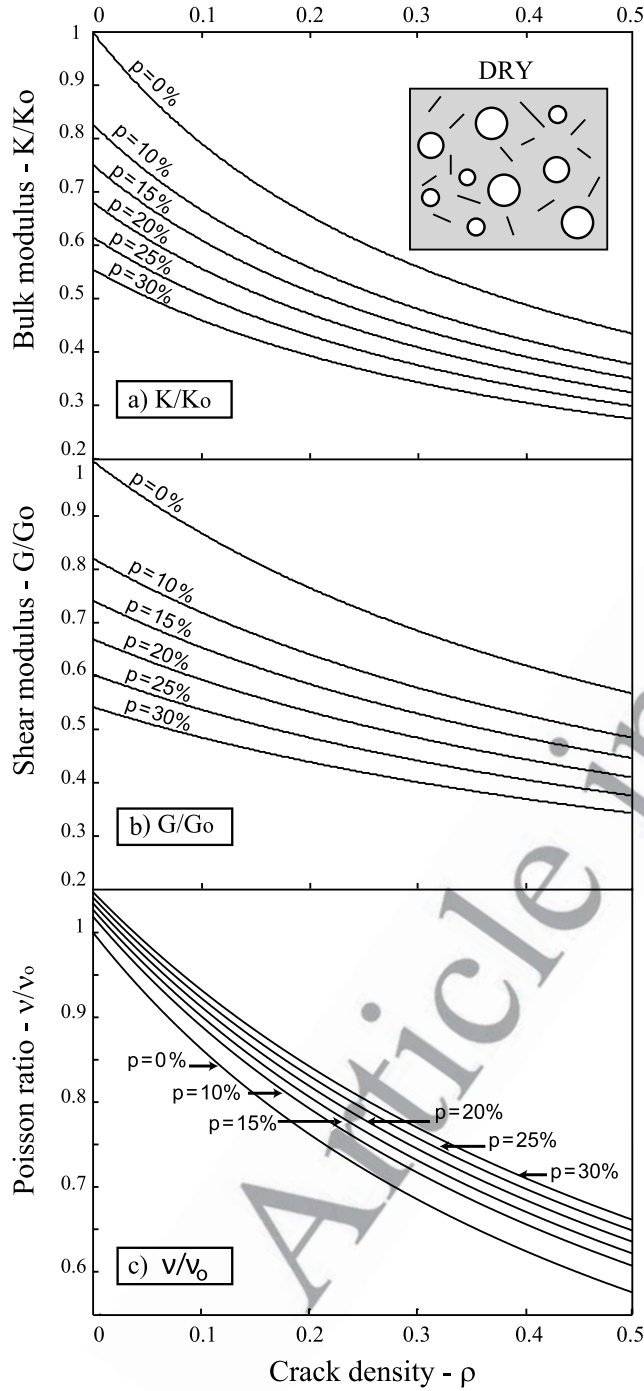


**Figure 5.** Effective elastic moduli of an idealized dry rock made of a mixture of penny-shaped cracks and spherical pores. (a) Effective bulk modulus  $K/K_o$ , (b) effective shear modulus  $G/G_o$ , and (c) effective Poisson ratio  $\nu/\nu_o$  plotted versus crack density  $\rho$  (range [0–0.5]). The curves are given at fixed porosity  $\phi$ , which varies from  $\phi = 0\%$  to  $\phi = 30\%$ . The bulk and shear moduli of the dry matrix ( $K_o$ ,  $G_o$ ) are summarized in Table 2.

379 the fluid compressibility, and the pore geometry. For a  
380 spherical pore, *Shafiro and Kachanov* [1997] showed that

$$\delta_s = \frac{2 E_o / K_f - 3(1 - 2\nu_o)}{9(1 - \nu_o)}. \quad (7)$$

For liquid water ( $K_f \simeq 2$  GPa) and elastic constants equal to 382  
 $E_o = 40$  GPa and  $\nu_o = 0.24$ ,  $\delta_s$  is equal to 5.4. 383

### 3.2. Effective Moduli of Dry Rock 384

[19] In the dry case, the stress perturbations due to the 385  
presence of spheroidal pores is taken into account and  $\Gamma =$  386  
 $1 - p$ . Parameters  $\delta$  and  $\delta_s$  are very large. Thus, from 388  
equation (2), the effective shear modulus  $G$  (which can be 389  
directly inverted from the  $S$  wave velocities), and the effective 390  
bulk modulus  $K$  (which can be directly inverted from a 391  
combination of the  $P$  and  $S$  wave velocities), can be derived as

$$\frac{K_o}{K} = 1 + \frac{\rho}{1-p} \frac{h}{1-2\nu_o} \left\{ 1 - \frac{\nu_o}{2} \right\} + \frac{p}{1-p} \frac{3(1-\nu_o)}{2(1-2\nu_o)}, \quad (8)$$

$$\frac{G_o}{G} = 1 + \frac{\rho}{1-p} \frac{h}{1+\nu_o} \left\{ 1 - \frac{\nu_o}{5} \right\} + \frac{p}{1-p} \frac{15(1-\nu_o)}{7-5\nu_o}, \quad (9)$$

where  $K_o$  and  $G_o$  are the bulk and shear moduli of the crack- 395  
and porosity-free matrix. Note that a dry effective modulus 396  
is also called a dry frame modulus, it is also called the 397  
drained modulus in quasi-static poroelasticity theory. The 398  
evolution of the elastic moduli  $K/K_o$ ,  $G/G_o$ , and  $\nu/\nu_o$  are 399  
plotted versus the crack density for different porosity values 400  
(range  $\phi = 0-30\%$ ) on Figures 5a, 5b, and 5c, respectively. 401  
Input data for the solid matrix are detailed in Table 2. 402

[20] The crack density being constant, a decrease in 403  
porosity induces a moderate increase of both the effective 404  
bulk and shear moduli while the Poisson ratio  $\nu$  decreases 405  
slightly. Reciprocally, at a given porosity, an increase of 406  
the crack density reduces the bulk and shear moduli. 407  
However, the Poisson ratio (Figure 5c) is affected in a 408  
different manner by cracks and decreases with increasing 409  
crack density. Note that the effects of cracks and pores are 410  
opposite on  $\nu/\nu_o$ : An increase of crack density reduces  $\nu/\nu_o$ , 411  
whereas an increase of porosity increases  $\nu/\nu_o$ . 412

### 3.3. Effective Moduli of Fluid-Saturated Rock 413

[21] In the wet case, the bulk and shear moduli can also 414  
be derived from equation (2) and can be expressed as 415

$$\frac{K_o}{K} = 1 + \rho \frac{h}{1-2\nu_o} \left\{ 1 - \left[ 1 - \left( 1 - \frac{\nu_o}{2} \right) \frac{\delta}{1+\delta} \right] \right\} + p \frac{3(1-\nu_o)}{2(1-2\nu_o)} \cdot \left\{ 1 - \frac{1}{1+\delta_s} \right\}, \quad (10)$$

$$\frac{G_o}{G} = 1 + \rho \frac{h}{1+\nu_o} \left\{ 1 - \frac{2}{5} \left[ 1 - \left( 1 - \frac{\nu_o}{2} \right) \frac{\delta}{1+\delta} \right] \right\} + p \frac{15(1-\nu_o)}{7-5\nu_o}. \quad (11)$$

In this case, the bulk and shear moduli are functions of the 418  
elastic properties of the matrix, the porosity  $p$ , the crack 420

**Table 2.** Bulk Modulus  $K_o$  and Shear Modulus  $G_o$  of the Wet and t2.1  
Dry Matrix (Crack- and Porosity-Free)<sup>a</sup>

	Solid Matrix Dry	Solid Matrix Wet	Fluid
$K_o$ , GPa	21.3	25.8	2
$G_o$ , GPa	18	16.2	0

<sup>a</sup> $K_o$  and  $G_o$  were calculated from the velocities data, assuming that the 421  
crack density  $\rho = 0$  when the velocities reach maximum values during the 422  
experiments. These values are used in the effective medium model "cracks 423  
and pores." 424

t2.5

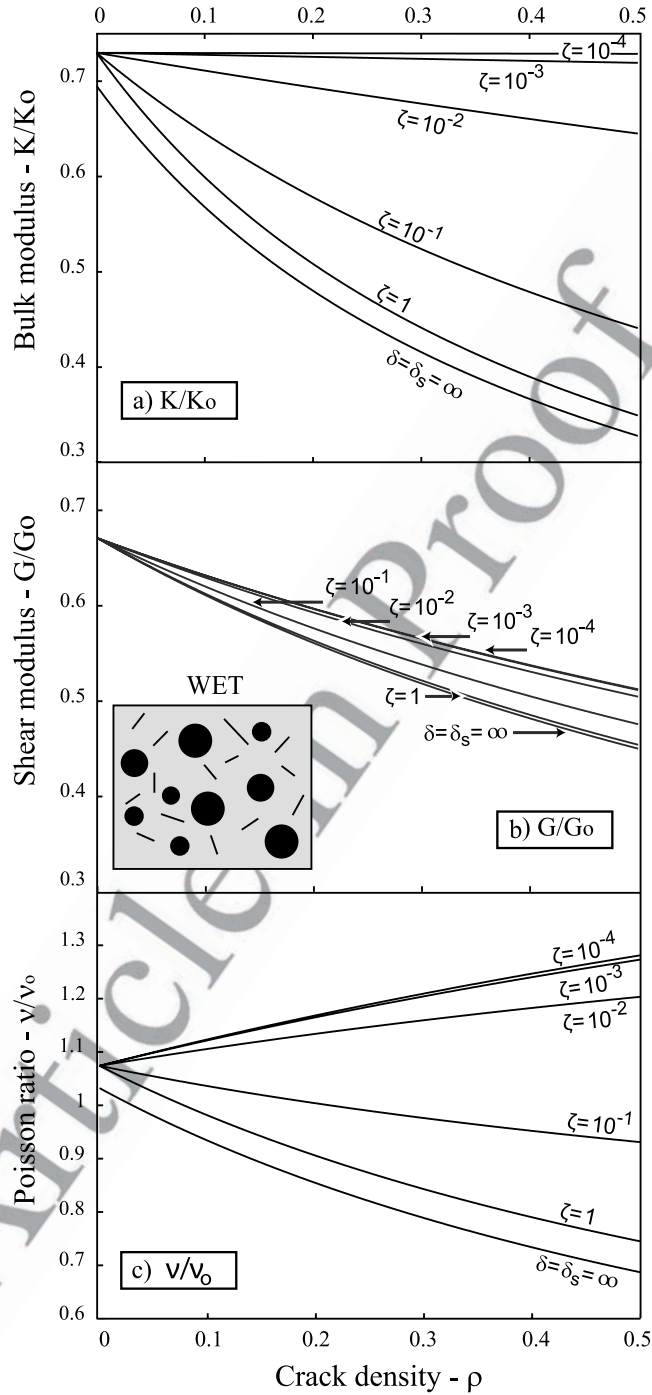


**Figure 6.** Effective elastic moduli of an idealized wet rock made of a mixture of penny-shaped cracks and spheroidal pores. (a) Effective bulk modulus  $K/K_o$ , (b) effective shear modulus  $G/G_o$ , and (c) effective Poisson ratio  $\nu/\nu_o$ , plotted versus crack density  $\rho$  (range [0–0.5]). The curves are given at fixed aspect ratio  $\zeta$ , which varies from  $\zeta = 1$  to  $\zeta = 10^{-4}$ . In these plots the porosity is constant and  $\phi = 20\%$ . The bulk and shear moduli of the wet matrix ( $K_o$ ,  $G_o$ ) are summarized in Table 2.

421 density  $\rho$ , and the aspect ratio  $\zeta$  (which affects the saturation  
 422 parameter  $\delta$ ). As in the dry case, the bulk and shear moduli  
 423 are inversely proportional to both the porosity and the crack  
 424 density. A new important parameter to be taken into  
 425 consideration here is the aspect ratio  $\zeta$ . Figures 6a, 6b,  
 426 and 6c show the evolution of both the bulk and shear

moduli ( $K/K_o$ ,  $G/G_o$ ) and the Poisson's ratio  $\nu/\nu_o$  versus the  
 427 crack density for different values of aspect ratio  $\zeta$ . The  
 428 porosity was fixed to 20%, and the matrix parameters are  
 429 summarized in Table 2. For a fluid-saturated rock and an  
 430 aspect ratio  $\zeta < \sim 10^{-3}$  the bulk and shear moduli decrease  
 431 as  $\zeta$  increases. Note that the controlling parameters is  $\delta$ . It is  
 432



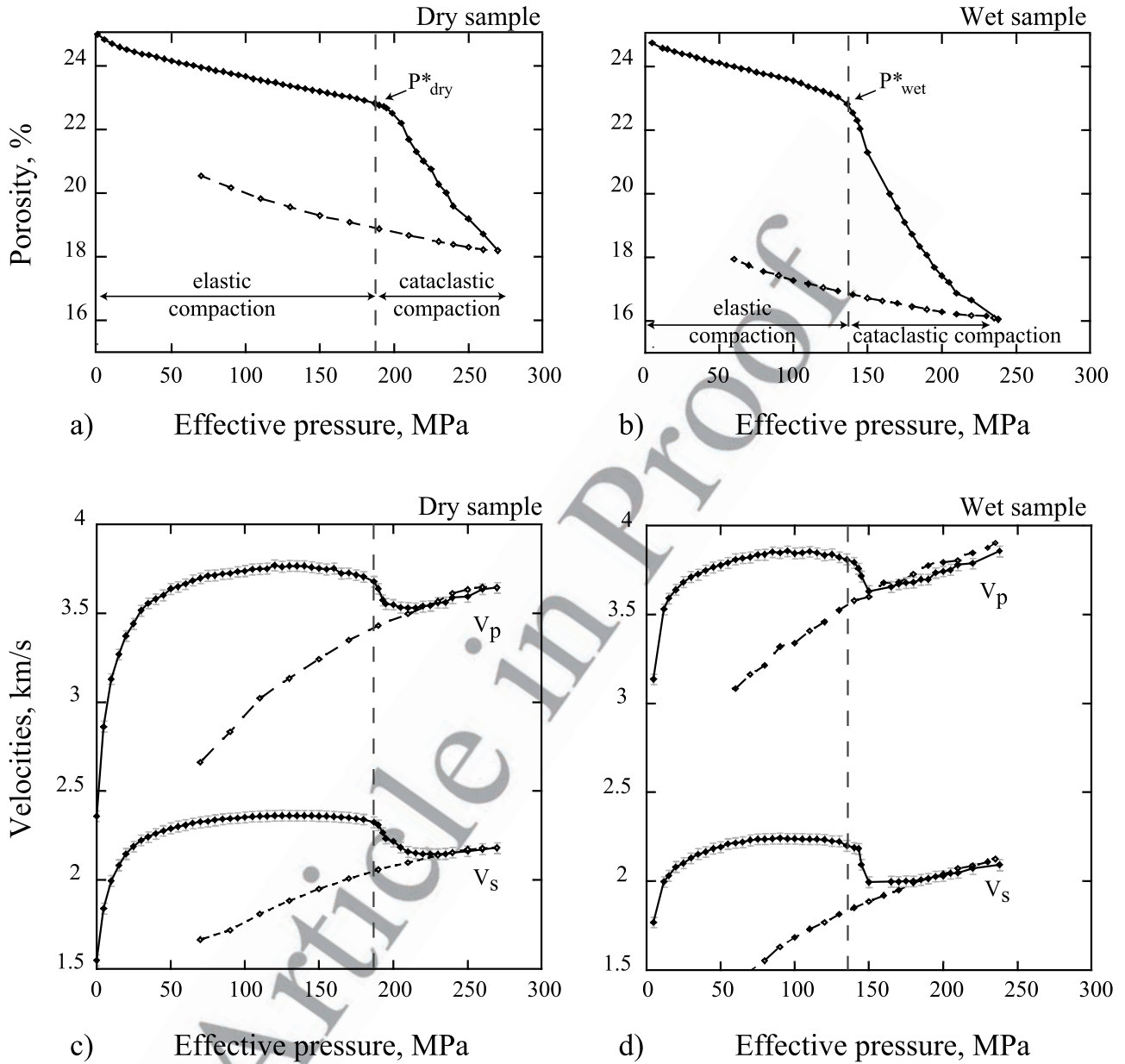


**Figure 7.** (a) and (b) Mechanical data for the dry and wet specimens. The porosity reduction is plotted versus effective pressure. The critical pressure  $P^*$  indicates the beginning of pore collapse and grain crushing.  $P^*$  is lower in the wet specimen than in the dry specimen, which is explained by chemo-chemical weakening effects. The unloading is plotted as dashed lines. (c) and (d) Velocity measurements for the dry and wet specimens. The elastic wave velocities  $P$  and  $S$  are plotted versus the effective pressure. At the critical pressure  $P^*$ , the velocities decrease because of grain crushing and pore collapse. Note that at pressure  $P \simeq 220$  and  $P \simeq 160$ , in the dry and wet specimens, respectively, the velocities increase again. The unloading is plotted as dashed lines.

433 equivalent to increase  $\delta$  by increasing  $\zeta$  or decreasing  $K_f$ .  
 434 The effect is the strongest (1) for the bulk modulus when  
 435 compared to the shear modulus and (2) in the limiting cases  
 436  $\zeta = 1$  (cracks are no longer cracks but spheres) or  $\delta = \delta_s = \infty$   
 437 (dry medium). The evolution of Poisson's ratio  $\nu/\nu_o$  is very  
 438 different compared to the dry case (Figure 6c): (1) if  $10^{-1} <$   
 439  $\zeta < 1$ ,  $\nu/\nu_o$  decreases slightly as  $\rho$  increases; and (2)  
 440 however, if  $10^{-4} < \zeta < 10^{-2}$ , the Poisson's ratio increases as  
 441 crack density increases. Such a behavior was also predicted

by the differential self-consistent model of *Le Ravalec and* 442  
*Guéguen* [1996]. 443

## 4. Results 445

### 4.1. Porosity Reduction Versus Pressure 446

[22] In the following, we use the convention that com- 447  
 pressive stresses and compactive strains are positive. Pore 448  
 pressure is denoted by  $P_p$  and the difference between 449

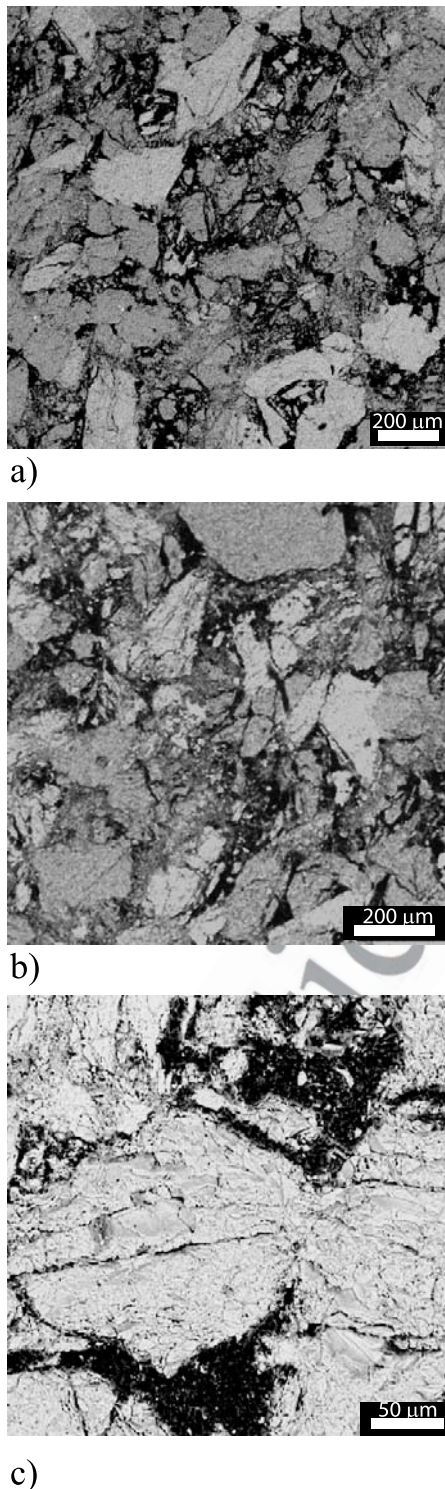


**Figure 8.** SEM micrograph (backscattered) of Bleurswiler sandstone. Epoxy-filled pores appear in black. (a) and (b) Pictures of the specimens deformed under dry condition. Crushed grains and cement fragments fill pore space, which result in large decrease of the porosity. (c) Fractured grains at grain-grain contacts.

confining pressure  $P_c$  and pore pressure is referred to as “effective pressure”  $P$ .

[23] Figures 7a and 7b show the evolution of porosity versus effective pressure for the dry and wet experiments, respectively. In both cases, at  $P < P^*$ , porosity reduction shows a linear dependence with effective pressure. On both curves, the inflection point,  $P^*$ , corresponds to the onset of grain crushing and pore collapse [Zhang *et al.*, 1990, Wong *et al.*, 1997], equal to 180 and 135 MPa, in the dry and wet experiment, respectively. Beyond  $P^*$ , accelerating inelastic volume compaction occurs due to extensive grain crushing, grain displacement, and pore collapse. Although there are a number of common pressure-dependent features on the two plots, the water-saturated sample is much weaker than the dry one. Such a difference in stress/strain response is probably caused by chemical weakening effects and stress corrosion due to presence of a chemically active pore fluid and has already been observed in previous experiments [Michalske and Freiman, 1981; Read *et al.*, 1995; Baud *et al.*, 2000a]. Following Baud *et al.* [2000a], the water-weakening effect on grain crushing can be expressed as  $P_{\text{wet}}^*/P_{\text{dry}}^* = (\gamma'/\gamma)^{3/2}$ , where  $\gamma$  and  $\gamma'$  are the specific surface energies of the dry and wet matrices, respectively. Our experimental results yield to  $\gamma'/\gamma = 0.82$ , a value in the range of those observed in Darley Dale, Gosford, and Boise sandstones reported by Baud *et al.* [2000a].

#### 4.2. Elastic Wave Velocities Data

[24] Figures 7c and 7d present the evolution of  $P$  and  $S$  wave velocities with effective pressure for the dry and wet experiment, respectively. A low effective pressure, up to 50 MPa,  $V_p$  and  $V_s$  increase drastically with pressure. Then for  $50 < P < P^*$ , the rate of increase in velocities is very small. Such a behavior in porous rocks has been reported by Lo *et al.* [1986]; Ayling *et al.* [1994]; Prasad and Manghnani [1997] and is interpreted by the closure of preexisting cracks and pores with small aspect ratios.

[25] However, at  $P^*$ , in dry or wet conditions and although porosity decreases, both  $P$  and  $S$  wave velocities drop sharply and decrease by several percent. This can only be explained by the nucleation and/or propagation of newly formed cracks appearing at high pressure. While pore collapse and porosity reduction tend to increase elastic wave velocities, newly formed cracks due to grain crushing tend to decrease the velocities. At first, increased damage and newly formed cracks play a dominant role. This result is consistent with the effective medium theory developed in section 3. Beyond  $P^*$ , Figures 7c and 7d show clear inflection points, at  $P \simeq 220$  MPa and  $P \simeq 160$  MPa in the dry and wet cases, respectively, where velocities start to increase again. At this point, the newly formed cracks are progressively being closed and the material becomes stiffer again.

[26] Velocities measured during depressurization (dashed lines on the plots) remain lower than those measured during pressurization, demonstrating the extensive damage accumulation as cracks reopen and propagate during unloading.

#### 4.3. Microstructural Observations

[27] Detailed microstructural analysis was performed on the dry sample using scanning electron microscopy (SEM). To prepare SEM sections, samples  $20 \times 40$  mm in size were cut parallel to the long specimen axis. Sections were



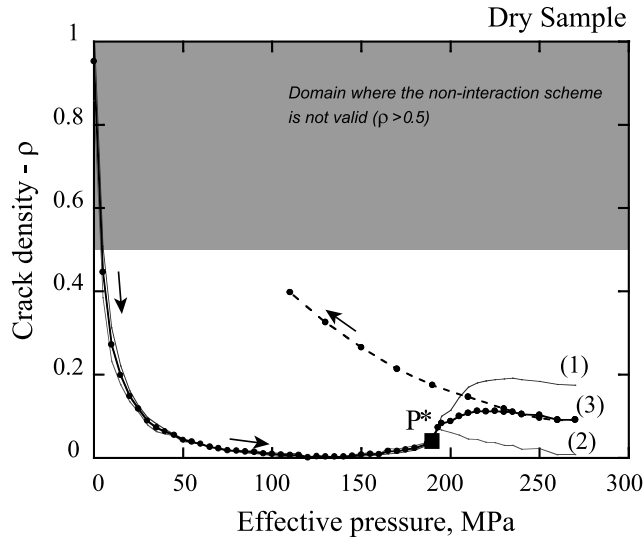


**Figure 9.** Evolution of crack density as a function of the effective pressure found in the dry specimen. Curves 1 and 2 show  $\rho$  values inverted from equation (9) ( $G$  modulus) and (8) ( $K$  modulus), respectively. Curve 3 shows the average between these two values of  $\rho$ . The beginning of pore collapse and grain crushing  $P^*$  is associated with an increase of the crack density. Curves 1 and 2 start to diverge at  $P^*$ , which may be explained by a mechanism of rolling contacts. The unloading is shown as a dashed line.

510 impregnated with epoxy and subsequently polished and  
511 gold coated.

512 [28] Thin sections do not reveal zones of localized  
513 crushing. Figures 8a and 8b are SEM micrographs of the  
514 deformed sample and illustrate the extensive grain crushing  
515 that took place during deformation (compare Figures 8a and  
516 8b with Figure 1b). Grain fragments fill up the existing  
517 pores leading to a large decrease in the porosity. Crack  
518 nucleation takes place at grain-grain contacts (Figure 8c),  
519 resulting in cracks at a scale with the original grain size.  
520 Moreover the crushing of some grain produces small micro-  
521 cracks and the scale of the fine produced is of the order of  
522 few microns (Figures 8a and 8b). Note that after unloading  
523 the rock was still cohesive.

## 525 5. Interpretations

### 526 5.1. Crack Density Evolution as Inferred From Elastic 527 Wave Velocities Variations

528 [29] The effective shear and bulk moduli  $GK$  are directly  
529 inverted from elastic wave velocities data using

$$G = \psi V_s^2 \quad \text{and} \quad K = \psi \left( V_p^2 - \frac{4}{3} V_s^2 \right).$$

532 [30] The bulk density of the rock  $\psi$  is corrected from  
533 porosity variations, with  $\psi = \psi_o(1 - p)$  and  $\psi_o = 2.6 \cdot 10^3 \text{ kg}$   
534  $\text{m}^{-3}$ . We assume that the crack porosity variation is negli-  
535 gible compared to the overall porosity. When velocities  
536 reach maximum values: at  $P \simeq 140 \text{ MPa}$  and  $P \simeq 100 \text{ MPa}$   
537 in the dry and wet experiment, respectively (Figure 7), the

rock is considered to be crack free ( $\rho = 0$ ) and the porosity is  
538 known. Then the shear and bulk moduli of the crack- and  
539 porosity-free matrix ( $K_o G_o$ ) can be estimated. Those values  
540 are reported in Table 2.

#### 541 5.1.1. Dry Experiment

542 [31] In the dry case, the effective medium model (pores  
543 and cracks) gives two independent relations (equations (8)  
544 and (9)) for a single crack parameter: the crack density. On  
545 Figure 9, the evolution of crack density is plotted versus  
546 pressure. Curve 1 plots  $\rho$  values inferred from  $S$  wave data  
547 (equation (9)) while curve 2 plots  $\rho$  values inferred from a  
548 combination of  $P$  and  $S$  waves data (equation (8)). Curve 3  
549 plots the average of  $\rho$  obtained from those two values.  
550 Initially, crack density  $\rho$  decreases from 1 to 0 as the  
551 confining pressure  $P$  is raised from 0 to 50 MPa. Since  
552 the associated porosity reduction in this part of the loading  
553 path is small ( $\sim 1\%$ ), the crack density decrease can be  
554 mainly attributed to viscoelastic closures of preexisting  
555 cracks and pores with small aspect ratio. Note that the  
556 agreement between the values inferred from equations (8)  
557 and (9) is excellent up to  $P^*$ .

558 [32] When pore collapse and grain crushing take place  
559 (at  $P = P^*$ ), the crack density  $\rho$  raises from 0 to a mean  
560 value of 0.1 (curve 3). An anomalous feature just beyond  
561  $P^*$  is that crack densities inferred from equations (8) and  
562 (9) become different: Inversion of  $G$  moduli gives a  $\rho$   
563 value close to 0.2, whereas inversion of  $K$  moduli data gives a  $\rho$   
564 value closer to 0.05. This discrepancy will be further  
565 analyzed in section 5.2. During depressurization (dashed  
566 lines), crack density increases drastically, showing not only  
567 crack reopening, but permanent damage accumulation.

#### 568 5.1.2. Fluid-Saturated Experiment

569 [33] In the wet experiment, both crack density  $\rho$  and  
570 average aspect ratio  $\zeta$  can be derived from the  $S$  and  $P$  wave  
571 data (equations (10) and (11)). Figure 10a plots crack  
572 density as a function of effective pressure. Figures 10a  
573 and 9 show some common features: a decrease of crack  
574 density from 1 to 0 in the first part of the loading path and  
575 then a jump at the beginning of pore collapse and grain  
576 crushing (at  $P \geq P^*$ ). However, in this experiment, the  
577 crack density inferred beyond  $P^*$  is equal to  $\rho = 0.4$ , which  
578 is a much higher value than in the dry case. Such a  
579 difference could be explained by chemomechanical effects,  
580 in the same way  $P^*$  has a much lower value.

581 [34] The evolution of average crack aspect ratio with  
582 effective pressure  $P$  is given in Figure 10b. As effective  
583 pressure is raised from 0 to 60 MPa, average crack aspect  
584 ratio increase exponentially from  $2 \times 10^{-2}$  to 0.5. Indeed,  
585 as pressure increases, the thinnest, most compliant cracks  
586 are first closed and this process leads to an increase of the  
587 average crack aspect ratio. When  $60 \text{ MPa} < P < 135 \text{ MPa}$ ,  
588 the crack density is fixed to 0, then from equations (10)  
589 and (11) there is an infinite number of solutions for  $\zeta$ .  
590 However, we can imagine that during this stage, all  
591 compliant cracks are closed, which leads, in theory, to  
592 an average aspect ratio close to 1. At  $P^*$ , the average  
593 aspect ratio decreases suddenly from 0.5 to  $\zeta = 3 \times 10^{-3}$ ,  
594 showing that new cracks were created at that point. Then  
595 beyond  $P^*$ ,  $\zeta$  decreases exponentially to reach a final  
596 value of  $3 \times 10^{-4}$  at 250 MPa. At the end of this  
597 experiment, the average crack aspect ratio is much lower  
598 than at the beginning (more than one order of magnitude).  
599



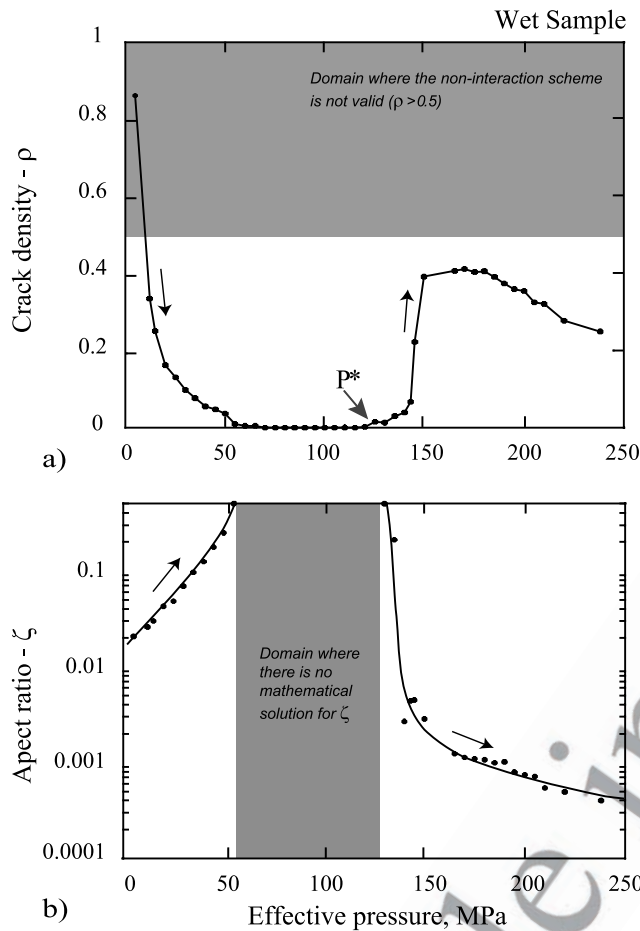


**Figure 10.** (a) Evolution of crack density and (b) aspect ratio as functions of the effective pressure in the wet specimen.  $P^*$  is associated with an increase of crack density higher than these found in Figure 8. The cracks created at the beginning of grain crushing ( $P > P^*$ ) have small aspect ratio,  $\zeta < 10^{-2}$ .

600 This implies that the mechanism of grain crushing create  
601 very thin cracks, which in agreement with our postmortem  
602 microstructural observations.

603 [35] These simple inversion results show that our effective  
604 medium model is a very powerful tool in order to  
605 describe the physical state of damage within a saturated  
606 rock.

## 607 5.2. Evolution of the Ratios $V_p/V_s$

608 [36] Taking into consideration  $V_p/V_s$  ratio leads to look at  
609 the rock from two different and complementary point of  
610 views.

### 611 5.2.1. Effective Medium Model

612 [37] Figure 11 plots the evolution of  $V_p/V_s$  ratios in the  
613 dry and wet experiments. On Figure 11, dots correspond to  
614 the experimental data, and solid lines represent the estimated  
615 values of  $V_p/V_s$  as inferred from the effective medium  
616 model, using the values for mean crack densities and aspect  
617 ratio shown on Figures 9 and 10. Recalling that  $V_p/V_s$  is a  
618 single function of Poisson ratio ( $(V_p/V_s)^2 = 2(1 - \nu)/1 -$   
619  $2\nu$ ), an increase in  $V_p/V_s$  is associated with an increase in  $\nu$   
620 and reciprocally. In the dry case, the  $V_p/V_s$  ratio of dry rock

increases substantially with increasing pressure (for  $P < 621$   
50 MPa). Again, this is a consequence of the viscoelastic 622  
closure of the preexisting cracks. In contrast, in the same 623  
range of pressure, when the rock is saturated with water, the 624  
 $V_p/V_s$  ratio decreases as effective pressure increases. Similar 625  
observations have been reported in previous experiments 626  
[Nur and Wang, 1989; Dvorkin and Walls, 2000]. In this 627  
pressure range, both in the dry and wet cases, the agreement 628  
between experimental data and predicted value from EM 629  
theory is good. Between 50 MPa and  $P^*$ , the  $V_p/V_s$  ratio is a 630  
constant which reflects the intrinsic rock properties:  $V_p/V_s =$  631  
1.59 and  $V_p/V_s = 1.72$  in the dry and wet case, respectively. 632  
 $V_p/V_s$  is larger in saturated conditions, which is in agreement 633  
with the result of Gassmann's static theory [Gassmann, 634  
1951] and previous experimental studies [Nur and Wang, 635  
1989]. 636

[38] Our experimental observations show that cataclastic 637  
compaction is associated with a sudden increase of the  $V_p/V_s$  638  
ratio ( $P \geq P^*$ ), this is observed both in wet and dry 639  
conditions (Figure 11). This increase in  $V_p/V_s$  ratio is only 640  
well predicted by the effective medium model in wet 641  
condition. This is explained by the additional crack param- 642  
eter  $\zeta$  used in model, and the dominant effect of average 643  
crack aspect ratio reduction ( $\zeta$  is in the range  $10^{-2} - 10^{-4}$  at 644  
 $P > P^*$ , see Figures 10b and 6c during closure of the newly 645  
formed cracks. 646

[39] In the dry case, however, our modeling does not 647  
predict an increase of the  $V_p/V_s$  ratio with increasing crack 648  
density but rather a slight decrease (Figures 11 and 5c). This 649  
last observation points out the limit of the previous effective 650  
medium model, which seems to be a better approximation in 651  
saturated conditions than in dry ones. This is probably due 652  
to the fact that stress interactions between cracks are larger 653  
in dry than saturated conditions, as water tends to act as a 654  
screen to stress perturbations. Thus the noninteraction 655  
approximation is likely to be a better approximation in 656

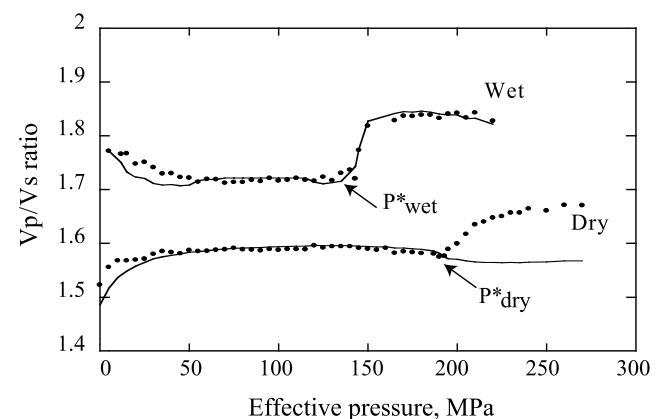


**Figure 11.** Evolution of the  $V_p/V_s$  ratio in the wet and dry specimens as functions of effective pressure. Dots are experimental data. The curves are estimations of  $V_p/V_s$  derived from the effective medium model “cracks and pores,” using crack density and aspect ratio shown in Figures 9 and 10. When pore collapse and grain crushing occur in the dry specimen, experimental data show an increase of  $V_p/V_s$ , which is not predicted by the effective medium model (see Figure 5c).

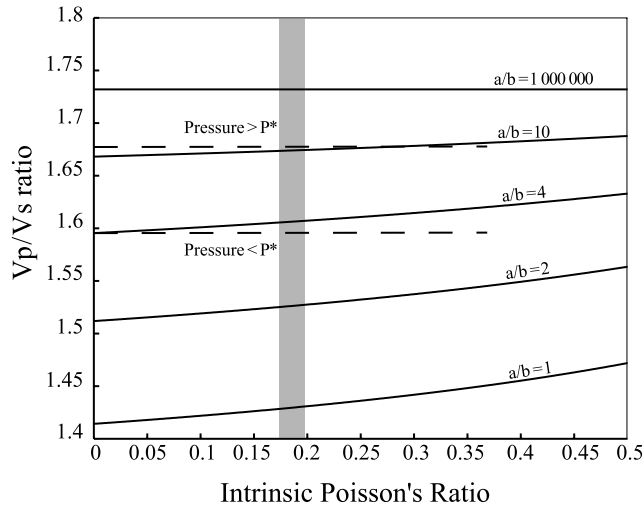


**Figure 12.** Digby's model. It is a granular model introducing  $b$  = bonding radius and  $a$  = contact radius. It gives the evolution of the ratio  $V_p/V_s$  as a function of the intrinsic Poisson's ratio of the grain, for different value of  $a/b$ . When  $P < P^*$ ,  $V_p/V_s = 1.59$ , which corresponds to  $a/b \simeq 3.5$ , with an intrinsic Poisson ratio fixed at  $\nu_o = 0.18$ , when  $P > P^*$ ,  $V_p/V_s = 1.67$ , and  $a/b \simeq 12$ . The physical explanation is that most grains are no more bonded at this second stage, which yields to lower values of  $b$ .

657 wet conditions. Additionally, and most importantly, the  
658 extra crack parameter  $\zeta$ , which is absent in the dry scheme,  
659 enables a finer description of the rock microstructural  
660 evolution, and increases the degree of freedom in the elastic  
661 wave velocity inversion from  $-1$  to zero.

### 662 5.2.2. Granular Model

663 [40] An alternative approach can be followed in order to  
664 understand the evolution of the  $V_p/V_s$  ratio in dry condi-  
665 tions. While the previous effective medium model con-  
666 siders the rock as a continuous matrix containing inclusions  
667 (here pores and cracks), a complementary view is to look at  
668 it as a discontinuous granular medium. In such way,  
669 Digby's [1981] dry granular medium model assumes that  
670 the rock is a homogeneous and isotropic granular medium,  
671 formed by randomly packed spherical grains. Neighboring  
672 spheres of radius  $R$  are initially firmly bonded across small,  
673 circular regions of average radius  $b$ . As the hydrostatic  
674 pressure increases in the medium, the spheres deform in  
675 such a way that the contact regions of all the neighboring  
676 spheres increases up to a radius  $a$  but remain flat and  
677 circular. In such a configuration,  $a \geq b$  and  $a, b \ll R$ . The  
678 simple case  $b = a$  corresponds to the usual Hertz-Mindlin  
679 result where the contact is infinitely rough and no slip is  
680 allowed. On the contrary, for an unconsolidated sand,  $b$   
681 goes to zero. Using Digby's [1981] model, the  $V_p/V_s$  ratio  
682 can be expressed as

$$\left(\frac{V_p}{V_s}\right)^2 = \frac{3\frac{a}{b}(2 - \nu_o) + 4(1 - \nu_o)}{\frac{a}{b}(2 - \nu_o) + 3(1 - \nu_o)}, \quad (12)$$

684 where  $\nu_o$  is the Poisson ratio of the solid grains. The  $V_p/V_s$   
685 ratio is now again a function of two independent

dimensionless quantities:  $(a/b)$  and  $\nu_o$ . The evolution of  
686 the  $V_p/V_s$  ratio is plotted as function of  $\nu_o$  for different  
687 values of  $a/b$  on Figure 12. Note that the  $V_p/V_s$  ratio depends  
688 weakly on initial  $\nu_o$  value. Figure 12 shows that the  
689 important parameter here is  $(a/b)$ . Digby's [1981] model  
690 predicts a maximum value of  $V_p/V_s \simeq 1.74$  when  $b \rightarrow 0$ .

691 [41] In dry conditions and in the range  $50 \text{ MPa} < P < P^*$ ,  
692  $V_p/V_s = 1.59$ . Using equation (12) and  $\nu_o \sim 0.18$  yields  $a/b \simeq$   
693  $3.5$ . At  $P > 220 \text{ MPa}$ ,  $V_p/V_s = 1.67$  is consistent with  $a/b \simeq$   
694  $12$ . Such an increase in  $(a/b)$  beyond  $P^*$  can be interpreted as  
695 a decrease in  $b$ , the bonding radius, which means the grains  
696 are less cemented. This is exactly what is expected from  
697 grain crushing, as it produces small uncemented grains  
698 (Figure 8). However, because only a fraction of the original  
699 grains have been crushed at the end of our experiments (the  
700 rock is still cohesive when retrieved from the pressure  
701 vessel), the maximum value of  $V_p/V_s = 1.74$  is not reached.  
702 The above interpretation allows us to add some comple-  
703 mentary comments to section 5.1.1. As pointed previously,  
704 Figure 9 shows that the dry crack density inverted from  
705 shear waves alone is larger than the one inverted from both  
706 compressional and shear waves. This, in fact, implies that  
707 the shear modulus  $G$  "sees" more damage than the bulk  
708 modulus  $K$  and suggests that the new grains contacts of the  
709 small uncemented grains produced by crushing resist better  
710 to compression than to shear, just as rolling contacts do.

### 712 5.3. Comparison With Other Studies Done on 713 Sandstones and Limestones

714 [42] Only few studies report the simultaneous evolutions  
715 of elastic wave velocities and porosity during pore collapse  
716 and grain crushing in porous rocks. Johnston and Toksöz  
717 [1980] and Nur and Simmons [1969] report experimental  
718 results obtained on Bedford limestone, a coarse-grained  
719 biogenetic limestone, poorly cemented by crystalline calcite  
720 with an initial porosity of 12%. Their experiments were  
721 performed in dry conditions and porosity reduction was  
722 calculated from axial strain measurements only, assuming  
723 that the deformation in the rock was isotropic. Figure 13  
724 summarizes their results: Porosity reduction (Figure 13a),  
725  $P$  wave velocities (Figure 13b), and  $S$  wave velocities  
726 (Figure 13c) are plotted versus effective pressure. The onset  
727 of pore collapse was reached at  $P^* \sim 100 \text{ MPa}$  (Figure 13a).  
728 In contrast to Bleurswiller sandstone, the  $P$  and  $S$  wave  
729 velocities both increased as  $P^*$  was reached. Again and as  
730 discussed throughout our study, the balance between the  
731 effects of an increase in crack density and a reduction of  
732 porosity can be invoked to explain the decoupling between  
733 the evolution of elastic wave velocities and porosity. In  
734 contrast with our experimental results obtained on a higher  
735 porosity rock, porosity reduction seemed to have a domi-  
736 nant effect on the evolution of elastic wave velocities.  
737 However, this would not longer be true if the rock's initial  
738 porosity was smaller, such as in the case of Solnhoffen  
739 limestone ( $p \sim 4\%$ ), as reported recently by Schubnel et al.  
740 [2005]. Therefore there must be a critical porosity under  
741 which the effect of porosity reduction becomes dominant  
742 during pore collapse. In sandstones, this critical porosity is  
743 high ( $>25\%$ ), whereas in limestones, it seems to be in  
744 between 4 and 12%. Such a difference between limestones  
745 and sandstones can be explained by the micromechanisms  
746 associated with pore collapse itself. In sandstones, pore

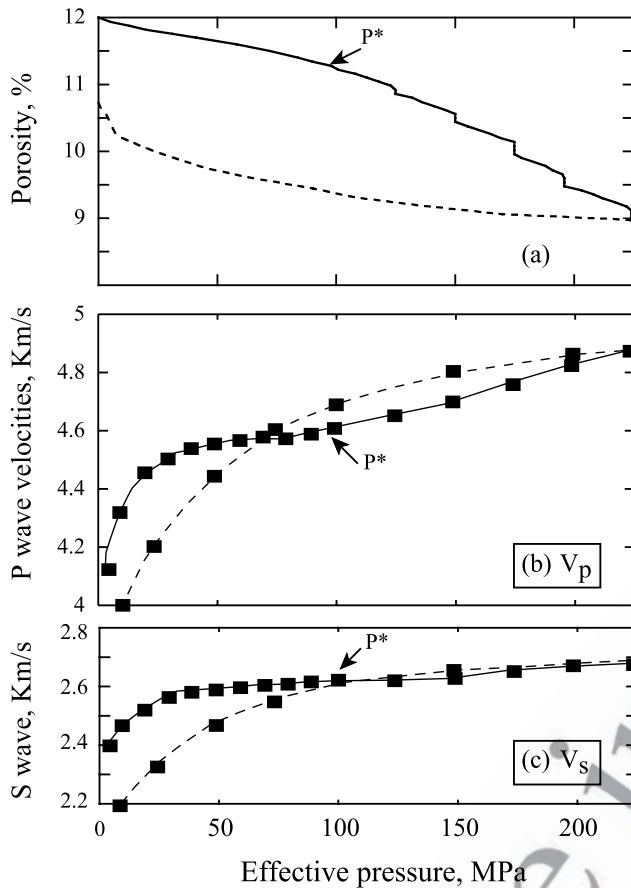


**Figure 13.** Dry hydrostatic compaction of Bedford limestone [from *Johnston and Toksöz, 1980*]. (a) Porosity reduction, (b)  $P$  wave velocities, and (c)  $S$  wave velocities as a function of effective pressure. In contrast with the experiments performed on Bleurswiller sandstone, the beginning of pore collapse ( $P^*$ ) is associated with an increase of the  $P$  and  $S$  wave velocities. The behavior of the velocities is explained by the micromechanisms of the deformation: In limestone, pore collapse is mainly due to calcite plasticity, and grain crushing is minor. Dashed lines represent unloading.

collapse is a result of grain crushing [*Zhang et al., 1990; Ménendez et al., 1996*] as porosity reduction is the consequence of the filling of pore space by fragmented grains. In limestones, however, pore collapse is the result of intragranular plasticity of calcite, i.e., twinning and dislocation glide [*Fredrich et al., 1989; Baud et al., 2000b; Vajdova et al., 2004; Schubnel et al., 2005*]. Hence cracking might be less pervasive and crack densities likely smaller. Nevertheless, the evolution of dynamic elastic properties during the deformation of limestones could probably be predicted successfully using the effective medium model pores and cracks that we presented in this study (see Figures 5 and 6).

[43] Finally, we would like to point out that both in limestones and sandstones, depressurization induces large decreases of elastic wave velocities (dashed lines on Figure 13), which proves the important role played by stress relief cracking in crack propagation. Such an observation was also performed on very low porosity calcic

rocks such as Carrara marble and Solnhoffen limestone [*Schubnel et al., 2005*] and even granites from the URL underground laboratory [*Collins and Young, 2000*]. This points out as well the limitations of postmortem microstructural investigations.

## 6. Conclusions

[44] Elastic  $P$  and  $S$  wave velocities have been measured during hydrostatic compression of the Bleurswiller sandstone in both dry and wet conditions. During the first part of the loading, the elastic wave velocities increased due to the closure of preexisting cracks, then the rate of increase in velocities was very small. Beyond a critical effective pressure  $P^*$ , pore collapse and grain crushing took place, which was readily confirmed by microstructural observations. However, and counter intuitively, both  $P$  and  $S$  wave velocities decrease at  $P^*$ . This could nevertheless be interpreted by showing that newly formed cracks produced by grain crushing played a dominant role on the evolution of elastic wave velocities.

[45] A new effective medium model [*Kachanov, 1993; Shafiro and Kachanov, 1997*] containing both penny shaped cracks and spheroidal holes, enabled us to interpret our experimental results in terms of the competition arising from an increase in crack density and a decrease of porosity during grain crushing and pore collapse. This model was proven to be a very powerful tool in order to quantify the physical state of the crack population within a rock. In particular, the model permitted retracing the evolution of both the crack density and the average aspect ratio from elastic wave velocities, and thus quantification of viscoelastic crack closure/opening, damage accumulation, and/or crack propagation during an entire loading cycle. Similar inversions were performed recently in nonporous rocks with equal success [*Benson et al., 2006; Schubnel et al., 2006*]. However, the model seems to be more reliable in wet conditions. In dry conditions, the model failed in predicting the observed increase of the  $V_p/V_s$  ratio during pore collapse and grain crushing. An alternative approach was then used, based on *Digby's* [1981] granular media modeling. It showed that the increase in  $V_p/V_s$  ratio can be analyzed as a transformation of the rock into a granular uncemented medium.

[46] The ratio  $V_p/V_s$  is a quantity frequently used in seismology and  $V_p/V_s$  anomalies have sometimes been recorded before and after earthquakes. For example, after the Antofagasta earthquake, an anomaly of  $V_p/V_s$  was observed [*Husen and Kissling, 2001; Koerner et al., 2004*]:  $V_p/V_s$  increased from 1.72 to a significant mean value of 1.77. *Husen and Kissling* [2001] suggested that the anomaly was fluid driven. Indeed, an increase of  $V_p/V_s$  at low temperature is, in general, interpreted in terms of fluid content for the sole reason that elastic wave velocities are dramatically affected by pore fluid properties. Compressional wave velocities are higher in fluid saturated rocks than in dry rocks, whereas the shear velocities are about the same which results in an overall increase of the  $V_p/V_s$  ratio [*Gassmann, 1951*]. However, the experimental results reported in this study show that grain crushing can induce an increase in  $V_p/V_s$  as well. In our case, the  $V_p/V_s$  ratio increased from 1.59 to 1.67 in the dry case, and from 1.72 to



826 >1.8 in the wet case (note that the analogy between field  
827 and experimental data is strictly valid for the dry case, for  
828 the wet case frequency effect due to high frequency used in  
829 the laboratory should be corrected). This result has been  
830 interpreted in the wet case as the result of both damage  
831 accumulation (increase in crack density) and crack geome-  
832 try (newly formed cracks with low aspect ratio  $<10^{-2}$ ). In  
833 the dry case, grains are becoming less and less cemented so  
834 that the rock is losing its cohesion. The physical implication  
835 is that  $V_p/V_s$  is not only a function of the saturation, but also  
836 of the microstructural state of the rock, i.e., of the crack  
837 density, the average crack aspect ratio, and the overall  
838 cohesion of the grains. This might have important implica-  
839 tions for the understanding of  $V_p/V_s$  anomalies in fault zones  
840 and fault gouges in the field.

841 [47] **Acknowledgments.** The technical skills of Guy Marolleau and  
842 Thierry Descamps have proved to be of major assistance, and both of them  
843 are greatly acknowledged. This work also benefited from discussion with  
844 many scientists. Among them, the authors would like to thank particularly  
845 Sergei Stanchits and Georg Dresen. The third author was supported by the  
846 Lassonde Institute, Toronto. Partial financial support for this work was  
847 provided by the CNRS.

## 848 References

- 849 Avseth, P., J. Dvorkin, G. Mavko, and J. Rykkje (1998), Diagnosing high-  
850 porosity sandstones for reservoir characterization using sonic and seismic  
851 data, paper presented at SEG Annual Convention, New Orleans, La.,  
852 Sept.
- 853 Ayling, M. R., P. G. Meredith, and S. Murrell (1994), Microcracking during  
854 triaxial deformation of porous rocks monitored by changes in rock physical  
855 properties, I. Elastic-wave propagation measurements on dry rocks,  
856 *Tectonophysics*, *245*, 205–221.
- 857 Baud, P., W. Zhu, and T.-F. Wong (2000a), Failure mode and weakening  
858 effect of water sandstone, *J. Geophys. Res.*, *105*, 16,371–19,390.
- 859 Baud, P., A. Schubnel, and T.-F. Wong (2000b), Dilatancy, compaction and  
860 failure mode in Solnhofen limestone, *J. Geophys. Res.*, *105*, 19,289–  
861 19,320.
- 862 Baud, P., E. Klein, and T.-F. Wong (2004), Compaction localization in  
863 porous sandstones: Spatial evolution of damage and acoustic emission  
864 activity, *J. Struct. Geol.*, *26*, 603–624.
- 865 Benson, P., A. Schubnel, S. Vinciguerra, C. Trovato, P. Meredith, and  
866 R. P. Young (2006), Modeling the permeability evolution of micro-  
867 cracked rocks from elastic wave velocity inversion at elevated isostatic  
868 pressure, *J. Geophys. Res.*, *111*, B04202, doi:10.1029/2005JB003710.
- 869 Bristow, J. R. (1960), Microcracks and the static and dynamic elastic con-  
870 stants of annealed and heavily cold-worked metals, *Br. J. Appl. Phys.*,  
871 *11*, 81–85.
- 872 Christensen, N. I., and H. F. Wang (1985), The influence of pore pressure  
873 and confining pressure on dynamic elastic properties of Berea sandstone,  
874 *Geophysics*, *50*, 207–213.
- 875 Collins, D. S., and R. P. Young (2000), Lithological controls on seismicity  
876 in granitic rocks, *Bull. Seismol. Soc. Am.*, *90*, 709–723.
- 877 Digby, P. J. (1981), The effective elastic moduli of porous rocks, *J. Appl.*  
878 *Mech.*, *48*, 803–808.
- 879 Dvorkin, J., and A. Nur (1996), Elasticity of high-porosity sandstones:  
880 Theory for two North Sea datasets, *Geophysics*, *61*, 1363–1370.
- 881 Dvorkin, J., and J. Walls (2000), Detecting overpressure from seismic  
882 velocity calibrated to log and core measurements, *Annu. Offshore*  
883 *Technol. Conf. OTC 11912*, *32*, 11 pp.
- 884 Fortin, J., A. Schubnel, and Y. Guéguen (2005), Elastic wave velocities and  
885 permeability evolution during compaction of Bleurswiller sandstone, *Int.*  
886 *J. Rock Mech. Min. Sci. Geomech.*, *25*, 873–889.
- 887 Fortin, J., S. Stanchits, G. Dresen, and Y. Guéguen (2006), Acoustic emis-  
888 sion and velocities associated with the formation of compaction bands in  
889 sandstone, *J. Geophys. Res.*, *111*, B10203, doi:10.1029/2005JB003854.
- 890 Fredrich, J. T., B. Evans, and T.-F. Wong (1989), Micromechanics of the  
891 brittle to plastic transition in Carrara marble, *J. Geophys. Res.*, *94*, 4129–  
892 4145.
- 893 Fredrich, J. T., G. L. Deitrick, J. G. Arguello, and E. P. de Rouffignac  
894 (1998), Reservoir compaction, surface subsidence, and casing damage:  
895 A geomechanics approach to mitigation and reservoir management, in  
896 *Eurorock-Rock Mechanics in Petroleum Engineering, SPE/ISRM 47284*,  
897 403–412, Soc. of Pet. Eng., Inc., Richardson, Tex.
- Gardner, G. H. F., M. R. J. Wyllie, and D. M. Droschak (1965), Hysteresis  
898 in the velocity-pressure characteristics of rocks, *Geophysics*, *30*, 111–  
899 116. 900
- Gassmann, F. (1951), Elasticity of high-porosity sandstone: Über die elas-  
901 tizität poroser medien, *Vierteljahrsschr. Nat. Ges. Zurich*, *96*, 1–23. 902
- Giles, M. R. (1997), *Diagenesis and Its Impact on Rock Properties: A*  
903 *Quantitative Perspective*, 520 pp., Kluwer Acad., Hingham, Mass. 904
- Hadley, K. (1976), Comparison of calculated and observed crack densities  
905 and seismic velocities in Westerly granite, *J. Geophys. Res.*, *81*, 3484–  
906 3493. 907
- Hashin, Z. (1988), The differential scheme and its application to cracked  
908 materials, *J. Mech. Phys. Solids*, *36*, 719–734. 909
- Husen, S., and E. Kissling (2001), Postseismic fluid flow after the large  
910 subduction earthquake of Antofagasta, Chile, *Geology*, *29*, 847–850. 911
- Johnston, D. H., and N. Toksöz (1980), Ultrasonic *P* and *S* wave attenua-  
912 tion in dry and saturated rocks under pressure, *J. Geophys. Res.*, *85*,  
913 925–936. 914
- Kachanov, M. (1980), Continuum model of medium with cracks, *J. Eng.*  
915 *Mech. Div.*, *106*, 1039–1051. 916
- Kachanov, M. (1993), Elastic solids with many cracks and related prob-  
917 lems, *Adv. Appl. Mech.*, *30*, 259–445. 918
- Kachanov, M., I. Tsukrov, and B. Shafiro (1994), Effective moduli of solids  
919 with cavities of various shapes, *Appl. Mech. Rev.*, *47*, S151–S174. 920
- Karner, S. L., F. M. Chester, A. K. Kronenberg, and J. S. Chester (2003),  
921 Subcritical compaction and yielding of granular quartz sand, *Tectonophy-*  
922 *sics*, *377*, 357–381. 923
- Klein, E., P. Baud, T. Reuschle, and T.-F. Wong (2001), Mechanical behav-  
924 iour and failure mode of Bentheim sandstone under triaxial compres-  
925 sion, *Phys. Chem. Earth, Part A*, *26*, 21–25. 926
- Koerner, A., E. Kissling, and S. A. Miller (2004), A model of deep  
927 crustal fluid flow following the  $M_w = 8.0$  Antofagasta, Chile, earth-  
928 quake, *J. Geophys. Res.*, *109*, B06307, doi:10.1029/2003JB002816. 929
- Lehner, F., and Y. Leroy (2004), Sandstone compaction by intergranular  
930 pressure solution, in *Mechanics of Fluid-Saturated Rocks*, *Int. Geophys.*  
931 *Ser.*, vol. 89, edited by Y. Guéguen, and M. Bouteica, pp. 115–168,  
932 Elsevier, New York. 933
- Le Ravalec, M., and Y. Guéguen (1996), High- and low- frequency elastic  
934 moduli for a saturated porous/cracked rock-Differential self-consistent  
935 and poroelastic theories, *Geophysics*, *61*, 1080–1094. 936
- Lo, T.-W., K. B. Coyner, and M. N. Toksöz (1986), Experimental determi-  
937 nation of elastic anisotropy of Berea sandstone, Chicopee shale, and  
938 Chelmsford granite, *Geophysics*, *51*, 164–171. 939
- Ménendez, B., W. Zhu, and T.-F. Wong (1996), Micromechanics of  
940 brittle faulting and cataclastic flow in Berea sandstone, *J. Struct. Geol.*,  
941 *18*, 1–16. 942
- Michalske, T. A., and S. W. Freiman (1981), A molecular interpretation of  
943 stress corrosion in silica, *Nature*, *295*, 511–512. 944
- Mollema, P. N., and M. A. Antonellini (1996), Compaction bands: A  
945 structural analog for anti-mode I crack in aeolian sandstone, *Tectonophy-*  
946 *sics*, *267*, 209–228. 947
- Mori, T., and K. Tanaka (1973), Average stress in matrix and average elastic  
948 energy of materials with misfitting inclusions, *Acta Meteorol.*, *21*, 571–  
949 574. 950
- Nur, A., and G. Simmons (1969), The effect of saturation on velocity in low  
951 porosity rocks, *Earth Planet. Sci. Lett.*, *7*, 183–193. 952
- Nur, A., and Z. Wang (1989), *Seismic and Acoustic Velocities in Reservoir*  
953 *Rocks*, vol. 1, *Experimental Studies, Geophys. Reprint Ser.*, vol. 10, Soc.  
954 of Explor. Geophys., Tulsa, Okla. 955
- O’Connell, R., and B. Budiansky (1974), Seismic velocities in dry and  
956 saturated rocks, *J. Geophys. Res.*, *79*, 5412–5426. 957
- O’Connell, R., and B. Budiansky (1977), Viscoelastic properties of fluid  
958 saturated cracked solids, *J. Geophys. Res.*, *82*, 5719–5736. 959
- Olsson, W. A. (1999), Theoretical and experimental investigation of com-  
960 paction bands in porous rock, *J. Geophys. Res.*, *104*, 7219–7228. 961
- Prasad, M., and M. H. Manghnani (1997), Effects of pore and differential  
962 pressure on compressional wave velocity and quality factor in Berea and  
963 Michigan sandstones, *Geophysics*, *62*, 1163–1176. 964
- Ramm, M. (1992), Porosity-depth trends in reservoir sandstones: offshore  
965 Norway, *Mar. Pet. Geol.*, *9*, 553–567. 966
- Read, M. D., M. R. Ayling, P. G. Meredith, and S. Murrell (1995), Micro-  
967 cracking during triaxial deformation of porous rocks monitored by  
968 changes in rock physical properties, II. Pore volumetry and acoustic  
969 emission measurements on water-saturated rocks, *Tectonophysics*, *245*,  
970 223–235. 971
- Rudnicki, J. W. (2004), Shear and compaction band formation on an elliptic  
972 yield cap, *J. Geophys. Res.*, *109*, B03402, doi:10.1029/2003JB002633. 973
- Salganik, R. L. (1973), Mechanics of bodies with many cracks, *Mech.*  
974 *Solids*, *8*, 135–143. 975
- Sayers, C. M., and M. Kachanov (1995), Microcracks induced elastic wave  
976 anisotropy of brittle rocks, *J. Geophys. Res.*, *100*, 4149–4156. 977

- 978 Schubnel, A., and Y. Guéguen (2003), Dispersion and anisotropy of elastic  
 979 waves in cracked rocks, *J. Geophys. Res.*, *108*(B2), 2101, doi:10.1029/  
 980 2002JB001824.
- 981 Schubnel, A., J. Fortin, L. Burlini, and Y. Guéguen (2005), Damage and  
 982 elastic recovery of calcite-rich rocks deformed in the cataclastic regime,  
 983 *J. Geol. Soc. London, Special Edition on High Strain*, 203–221.
- 984 Schubnel, A., P. Benson, B. Thompson, J. Hazzard, and R. P. Young  
 985 (2006), Quantify damage, saturation and anisotropy in cracked rocks  
 986 by inverting elastic wave velocities, *Pure Appl. Geophys.*, *163*, 947–  
 987 973, doi:10.1007/s00024-006-0061-y.
- 988 Scott, T. E., Q. Ma, and T. C. Røegiers (1993), Acoustic velocity changes  
 989 during shear enhanced compaction of sandstone, *Int. J. Rock Mech. Min.*  
 990 *Sci. Geomech.*, *30*, 763–769.
- 991 Shafiro, B., and M. Kachanov (1997), Materials with fluid-filled pores of  
 992 various shapes: Effective elastic properties and fluid pressure polariza-  
 993 tion, *Int. J. Solids Struct.*, *34*, 3517–3540.
- 994 Shapiro, S. (2003), Piezosensitivity of porous and fractured rocks, *Geophy-*  
 995 *sics*, *68*, 482–486.
- 996 Smits, R. M. M., J. A. de Wall, and J. F. C. van Kooten (1988), Prediction  
 997 of abrupt reservoir compaction and subsurface subsidence by pore col-  
 998 lapse in carbonates, *SPE Form. Eval.*, *3*, 340–346.
- 999 Vajdova, V., P. Baud, and T. Wong (2004), Compaction, dilatancy, and  
 1000 failure in porous carbonate rocks, *J. Geophys. Res.*, *109*, B05204,  
 1001 doi:10.1029/2003JB002508.
- Walsh, J. B. (1965), The effect of cracks on the compressibility of rocks, 1002  
*J. Geophys. Res.*, *70*, 381–389. 1003
- Wong, T.-F., C. David, and W. Zhu (1997), The transition from brittle 1004  
 faulting to cataclastic flow in porous sandstone: Mechanical deformation, 1005  
*J. Geophys. Res.*, *102*, 3009–3026. 1006
- Wong, T.-F., C. David, and B. Menéndez (2004), Mechanical compaction, 1007  
 in *Mechanics of Fluid-Saturated Rocks, Int. Geophys. Ser.*, vol. 89, edited 1008  
 by Y. Guéguen and M. Bouteica, pp. 55–114, Elsevier, New York. 1009
- Zhang, J., T.-F. Wong, and D. M. Davis (1990), Micromechanics of pres- 1010  
 sure-induced grain crushing in porous rocks, *J. Geophys. Res.*, *95*, 341– 1011  
 352. 1012
- Zimmerman, R., W. Somerton, and M. King (1986), Compressibility of 1013  
 porous rocks, *J. Geophys. Res.*, *91*, 12,765–12,777. 1014
- 
- J. Fortin and Y. Guéguen, Laboratoire de Géologie, Ecole Normale 1015  
 Supérieure, 24 rue Lhomond, 75005, Paris, France. (fortin@geologie. 1017  
 ens.fr) 1018
- A. Schubnel, Lassonde Institute, University of Toronto, 170 College 1019  
 Street, Toronto, ON, Canada M5S 3E3. 1020